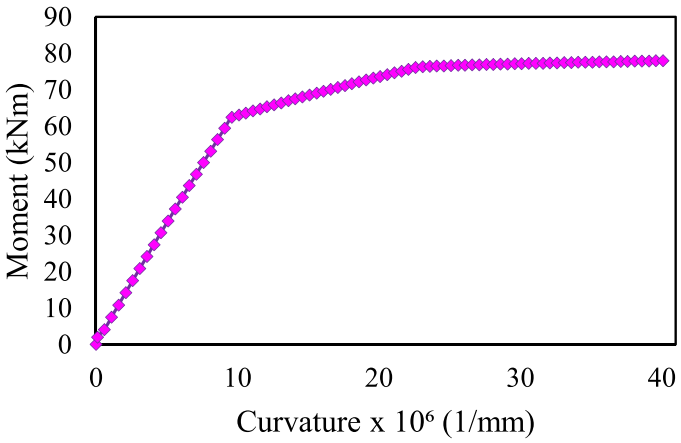

Fig. 7. M_a-χ relationship.

[1]).

The determination of the midspan displacement as a function of M_a was subsequently obtained using the principle of virtual work. As reference of the real and fictional schemes, the Eqs. (5) and (6) can be drawn,

$$M^R(z_1) = F\,z_1\,,\; M^f(z_1) = \frac{1}{2} \quad z_1, 0 \le z_1 < \frac{L}{3} \tag{5}$$

$$M^R(z_2) = \frac{F}{3}\frac{L}{3},\; M^f(z_2) = \frac{L}{6} + \frac{z_2}{2} \quad 0 \le z_2 \le \frac{L}{6} \tag{6}$$

and the δ determined as reported in Eq. (7),

$$\delta = 2\left(\int_0^{\frac{L}{3}} \frac{M^f(z_1)}{EM_{SE772}}\frac{M^R(z_1)}{J\left(M^R(z_1)\right)}dz_1 + \int_0^{\frac{L}{6}} \frac{M^f(z_2)}{EM_{SE772}}\frac{M^R(z_2)}{J\left(M^R(z_2)\right)}dz_2\right) \tag{7}$$

where: δ is the midspan deflection for B_SE772, $M^R(z_1)$ and $M^R(z_2)$ are the bending moments due to the real loading, $M^f(z_1)$ and $M^f(z_2)$ are the bending moments due to the virtual unitary loading, L is the effective beam length and $J(M^R(z_1))$ is the moment of inertia as a function of the bending moment due to the real moment. Shear contributions have been neglected.

3. Results and discussion

3.1. Compressive test

The crack pattern observed in the SE772_C-28 is deemed satisfactory per the criteria laid out in standard [26], as illustrated in Fig. 8. Table 3 presents a summary of the engineering properties of SE772 * , derived from the tests conducted on the cubic specimens. The obtained standard deviation aligns with results from compression tests on earth-based materials [5,6,33].

Table 3
Engineering properties of SE772 * .

Specimens	BD (kg/m^3)	C-28 (MPa)
SE772_C-28_1	2107.20	14.38
SE772_C-28_2	2084.83	13.62
SE772_C-28_3	2071.61	12.84
SE772_C-28_4	2048.89	10.04
Avg.±Std Dev.	**2078.13±24.41**	**12.72±1.89**

C-28: 28-day compressive strength value
BD: Bulk density after curing

3.2. Pull-out test

Despite the confinement offered by the SE cover at a minimum thickness of 12ø, all of the P_SE772 * _l_ ø specimens failed by splitting, as shown in Fig. 9. This is mainly due to: (i) the insufficient confinement provided by the SE, and (ii) absence of stirrups.

In Fig. 10, a comparison between the experimental results and the CEB-FIP MC90 [15] and CEB-FIP MC2010 [16] predictive models is presented in terms of bond stress-*vs*-slip relation.

In Fig. 10, the initial curved segment derived from the models corresponds to the phase where the ribs penetrate the mortar matrix, a process accompanied by micro-cracking. Experimental outcomes for this initial segment align well with model predictions, irrespective of the embedding length. Upon reaching τ_{max}, the declining phase begins, attributed to the splitting failure evident in these results.

Table 4 details a comparison between the τ_{max} observed for each specimen and the values predicted by the two models. For an embedding length of 10ø, τ_{max} shows a significant alignment with $\tau_{max,CEB\text{-}MC2010}$; the relative error for each specimen remains under 17%. Conversely, P_SE772 * _15ø _12 typically registers values higher than those anticipated by the models. Yet, a consistent pattern emerges, demonstrating that τ_{max} augments in tandem with the bonded length. As such, for embedding lengths exceeding 10ø, there is a pronounced alignment with the predictive model tailored for RC materials under optimal bond conditions. This suggests that presuming perfect adhesion between steel bars and SE is a plausible approximation—mirroring assumptions in traditional RC—given a sufficiently long bonded segment.

While the experimental bond stress at a 6 mm slip closely mirrors the standard proposed by CEB-MC90, the declining segment presents a gentler gradient in comparison to anticipated trajectories. This discrepancy may stem from residual bond stresses caused by concrete shearing between ribs. Future investigations are slated to offer a more in-depth characterization of the interplay between SE and steel rebars.

3.3. Four-point loading bending test

In Scenario S1, the horizontal LVDTs, which are affixed to the middle region of the beam, allow for the approximation of the theoretical cur-

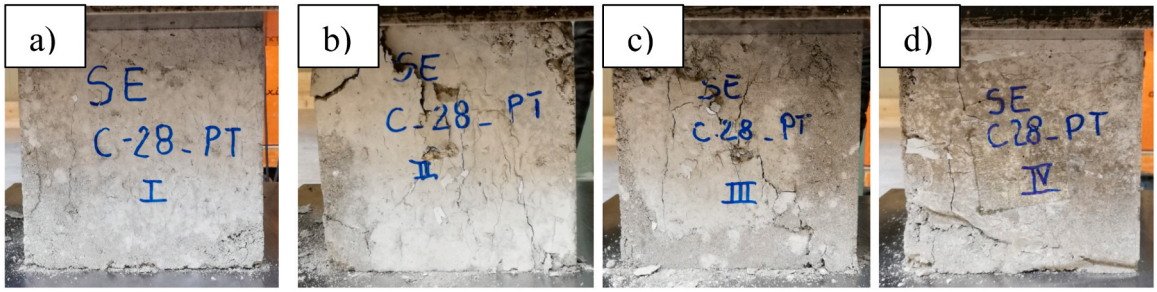

Fig. 8. Crack patterns of: a) SE772 * _C-28_1, b) SE772 * _C-28_2, c) SE772 * _C-28_3, d) SE772 * _C-28_4.

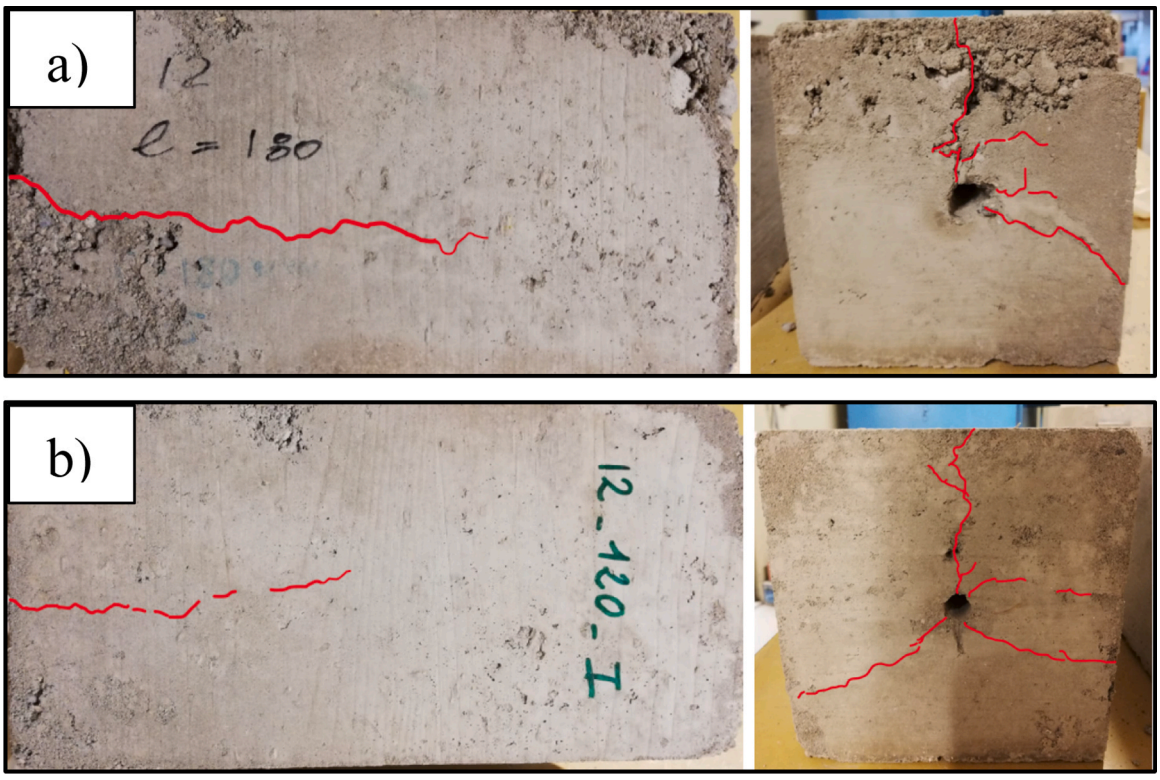

Fig. 9. Splitting failure mode for: a) P_SE772 * _10ø_12, b) P_SE772 * _15ø_12.

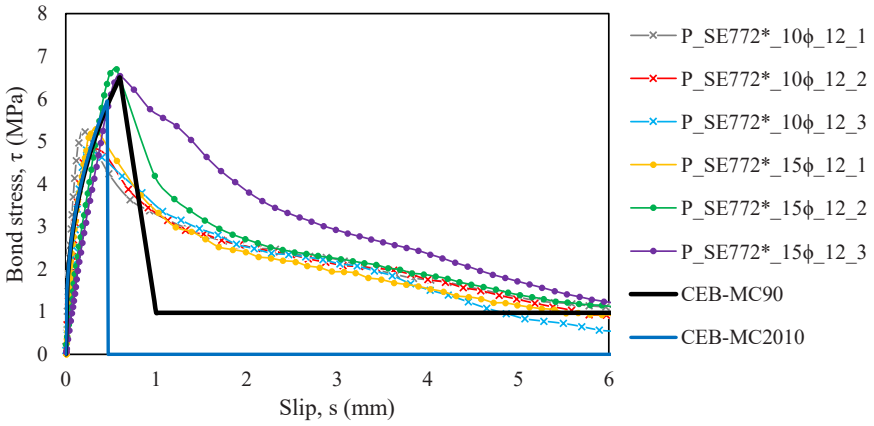

Fig. 10. Bond stress – slip relationship: comparison between experimental results and predictive models.

Table 4
Comparison between experimental and predictive models in terms of τ_{max}.

Specimens	τ_{max} (MPa)	$\tau_{max}/\tau_{max,CEB\text{-}MC90}$ (MPa)	$\tau_{max}/\tau_{max,CEB\text{-}MC2010}$ (MPa)
P_SE772 * _10ø_12_1	5.27	0.81	0.88
P_SE772 * _10ø_12_2	4.95	0.76	0.83
P_SE772 * _10ø_12_3	4.92	0.76	0.83
P_SE772 * _15ø_12_1	5.36	0.82	0.90
P_SE772 * _15ø_12_2	6.75	1.03	1.13
P_SE772 * _15ø_12_3	6.55	1.01	1.10

vature of the cross-section during loading and unloading cycles, see Eq. (8),

$$\chi = \frac{M_0}{EM_{SE772}\ J_{om}} + (\delta_{int} + \delta_{ext})\frac{1}{l_{cr}}\frac{1}{h} \tag{8}$$

where: M_0 is the midspan moment due to the self-weight load of the reinforced B_SE772, EM_{SE772} is the elastic modulus of the SE772 which is assumed as reported in [5], J_{om} is the moment of inertia of the homogenized cross section, δ_{int} is the extension at the intrados measured by horizontal LVDTs glued on the bottom fiber during the S1, δ_{ext} is the shortening at the extrados measured by horizontal LVDTs glued on the top fiber during the S1, l_{cr} is the characteristic length of the LVDT, and h is the height of the beam cross-section.

The Fig. 11 shows the total load applied to the beam (P1 + P2) *vs* the midspan deflection. The self-weight deflection contribution ($\delta = 0.93$ mm), computed according to the theory of elasticity, has been added to the measured midspan displacement. Furthermore, in Fig. 11 (a) is highlight a comparison between the experimental moment-curvature diagram and the M_a - χ relationship as defined in the model presented in Section 2.5.2. This comparison is intended to validate the theoretical diagram of Fig. 7 in the elastic field.

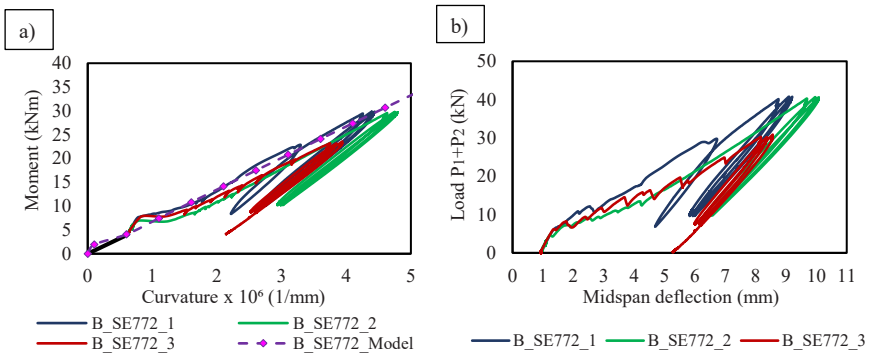

Fig. 11. a) Moment-Curvature diagram in S1 b) Load-midspan deflection diagram in S1.

At the end of S1, the S2 is set to measure the mechanical response of the beam as the load increases until to reach the complete failure, see Fig. 12. The self-weight offset has been considered in S2 too.

All beams in both phases (S1 and S2) display consistent trends, thereby validating the repeatability of the SE manufacturing process. Following the elastic phase, the reinforced SE beams demonstrates ductile behavior, attributable to the presence of the steel reinforcement. Notably, there's a distinct phase where the midspan deflection amplifies while the force remains constant. This behavior closely aligns with that observed in RC beams. The flexural performance metrics for the reinforced SE beams can be found summarized in Table 5.

For all beam samples, the first macro-cracks appear upon reaching the peak load in the midspan. All the samples display similar crack patterns. As seen in reinforced concrete beams, there is an almost homogeneous distribution of vertical cracks corresponding to the position of the steel stirrups embedded in the beam, as shown in Fig. 13. As the load increases, the cracks gradually widen and increase particularly in the neighboring of the supports. At the failure load, the cracks in the central region have an average length of 32 mm and a width of 2 $\pm$ 1 mm, while the cracks in proximity to the supports are characterized by an average length of 20 mm and a width of 0.2 $\pm$ 0.1 mm.

All the reinforced SE beams exhibited failure in a flexural mode. Initially, the steel bars in the bottom fiber undergo plasticization, a phenomenon further corroborated by the plateau observed in Fig. 12. This is followed by a compression failure in the top fiber, as illustrated in Fig. 14(a). The ultimate collapse of the reinforced SE beams arises once the steel bars in the bottom fiber break, as depicted in Fig. 14(b). This highlights a ductile failure, thus confirming the "good bond behavior" [15,16] between SE and steel bars as shown in Section 3.2. This corroborates the assumption of perfect adhesion adopted in Section 2.5.2.

A comparison between the analytical predictions and experimental results in terms of $P_1 + P_2 - \delta$ relationship is shown in Fig. 15. It should be noted that the model well approximates the experimental results in both the elastic and plastic fields. The maximum failure load provided by the model is 123.20 kN with a displacement δ of 50.95 mm. At the theoretical failure point, the SE strain is 3‰, while the steel in the in the lower tension zone reaches 12‰. The differences covered by the experiment are due to a twofold cause: (i) the maximum force of the model is lower due to an additional hardening effect near the failure, (ii) based on the experimentally observed failure domains, it is reasonable to assume the formation of a localized plastic hinge, enabling significant displacements under constant load.

Table 5
Load, Moment and midspan deflection peaks measured during the four-points loading bending test on reinforced SE beams.

Specimens	P_u (kN)	M_u (kNm)	δ (M_u) (mm)
B_SE772_1	139.04	92.08	97.16
B_SE772_2	135.88	90.08	90.92
B_SE772_3	133.80	88.76	85.33
Avg. ±Std Dev	**136.24±2.64**	**90.31±2.64**	**91.14±5.92**

P_u: ultimate load
M_u: ultimate moment
$\delta(M_u)$: Midspan displacement at ultimate moment

4. Conclusions

In this research, an experimental campaign was conducted to characterize the adherence between SE772 and steel bars. Subsequently, the flexural behavior of reinforced SE772 was examined through four-point loading bending tests. Due to the lack of predictive models for earthen structures, existing models designed for RC were employed. These models aimed to predict both the adherence between SE772 and steel bars and the load–displacement relationship of reinforced SE772 members under bending. The presented models were then validated against experimental results. From this research, several conclusions can be drawn:

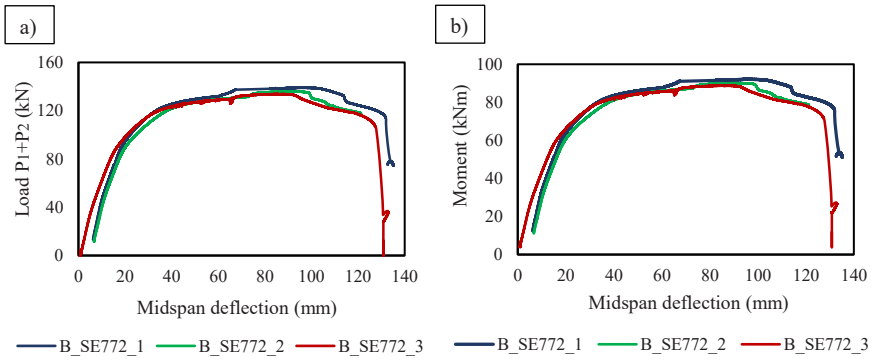

Fig. 12. a) Load-midspan deflection in S2, b) Moment-midspan deflection diagram in S2.

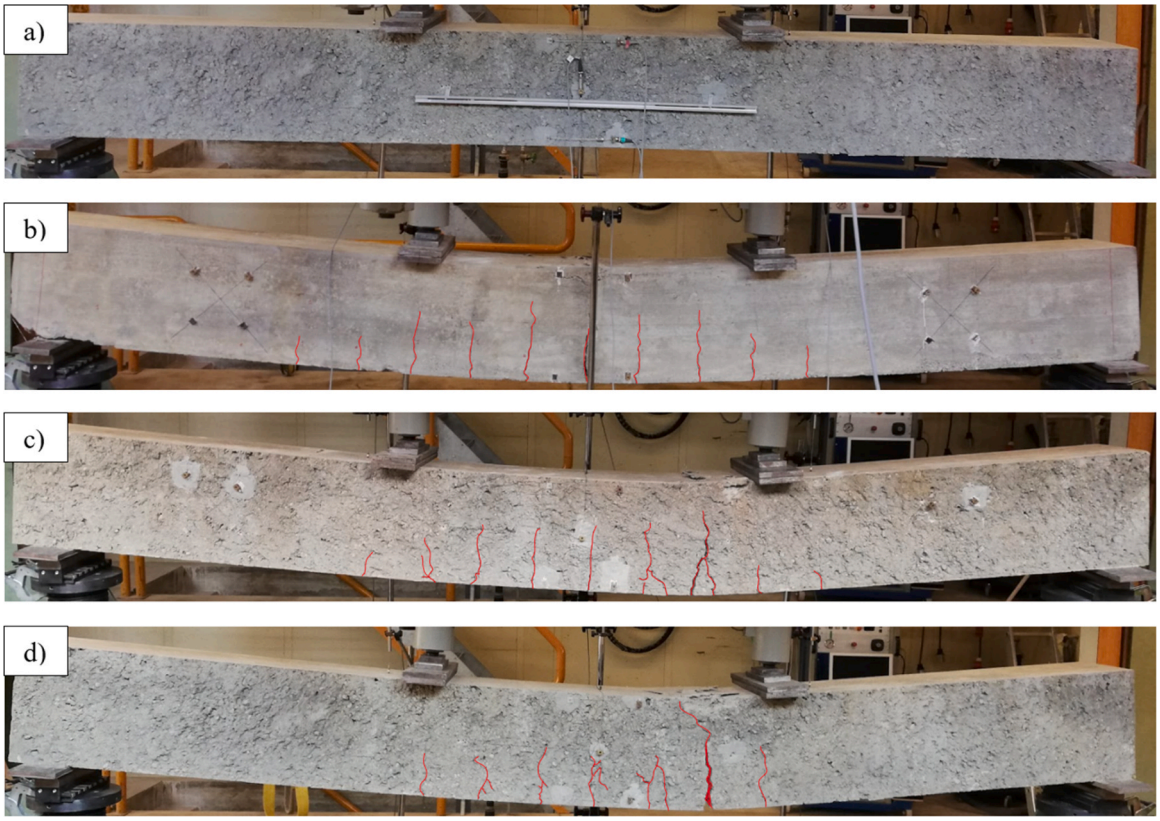

Fig. 13. a) Undeformed configuration. Crack pattern for: b) B_SE772_1, c) B_SE772_2, d) B_SE772_3.

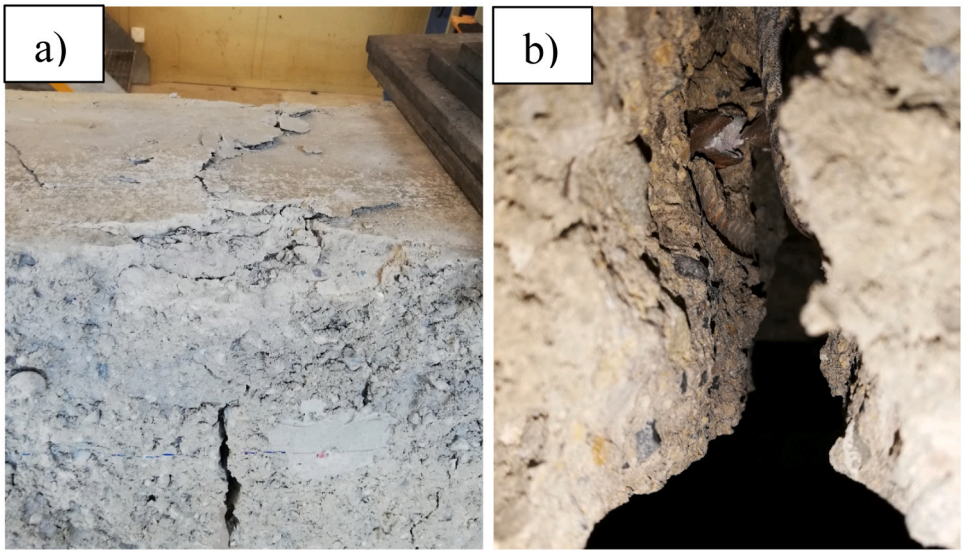

Fig. 14. a) SE failure in compression b) Steel failure.

1. A comparison of suitable predictive models for RC structures with experimental results from pull-out tests supports the hypothesis of perfect adhesion between steel bars and SE materials.
2. The model based on the stress-strain relationship, tailored for concrete, accurately anticipates the behavior of reinforced earth beams under bending. This suggests that the model has potential utility in designing steel-reinforced SE beams with an optimal reinforcement configuration to fulfill specific structural requirements. Moreover, the adoption of this model might address challenges related to limited understanding of the behavior of earthen materials and their interaction with steel reinforcement.

In conclusion, this study underscores the potential of projected steel-reinforced earthen materials. It also indicates that methodologies from existing RC structure models can be applied to reinforced SE structures, offering a potential avenue towards more sustainable and cost-efficient construction methodologies.

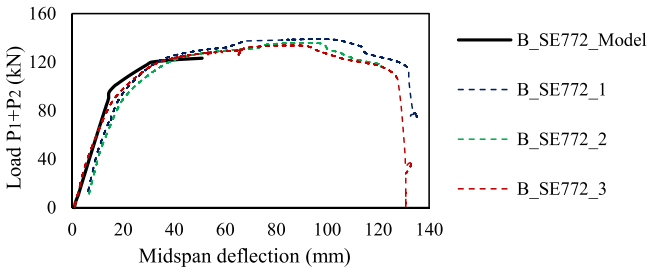

Fig. 15. Load P1 + P2 – midspan deflection relationship in comparison with B_SE772 model.

Declaration of Competing Interest

The authors declare that they have no known competing financial interests or personal relationships that could have appeared to influence the work reported in this paper.The authors declare that the present work has been realized in compliance with the Ethical Standards.

This study was funded by the aforementioned grant only.

Data Availability

Data will be made available on request.

Acknowledgments

Financial support from the HES-SO in the framework of the projects "NextEarthBuild – Une nouvelle génération d'éco-construction en terre d'excavation recycle – n° 98528" and "EcoAbri – Construction d'un abri t é moin en terre d'excavation et autres matériaux écologiques et indigènes en vue de la réalisation ultérieure d'un espace de rangement non chauffé – n° 108222" is gratefully acknowledged. Financial support from Innosuisse in the framework of the Project "Innosuisse – Shotearth: a sustainable excavated-soil based building material – n° 52127.1 IP-EE " is gratefully acknowledged as well. Financial support from the Italian Ministry of University and Research (MUR) in the framework of the projects PRIN 2022 "New eco-friendly building materials inspired by ancient constructions" (prot. 2022Y2RHHT; CUP E53D23003900006), FISA 2022-00183 "Earth-Tech") and "FAR Dipartimentale 2022–2023" (CUP: E93C22000590005 from University of Modena and Reggio Emilia are gratefully acknowledged. Luca Lanzoni is member of Gruppo Nazionale di Fisica Matematica (GNFM) of Istituto Nazionale di Alta Matematica (INdAM).

References

[1] Miccoli L, Müller U, Fontana P. Mechanical behaviour of earthen materials: A comparison between earth block masonry, rammed earth and cob. Constr Build Mater 2014;61:327–39. https://doi.org/10.1016/j.conbuildmat.2014.03.009.
[2] Morel JC, Mesbah A, Oggero M, Walker P. Building houses with local materials: means to drastically reduce the environmental impact of construction. Build Environ 2001;36:1119–26. https://doi.org/10.1016/S0360-1323(00)00054-8.
[3] Benhelal E, Zahedi G, Shamsaei E, Bahadori A. Global strategies and potentials to curb CO_2 emissions in cement industry. J Clean Prod 2013;51:142–61. https://doi.org/10.1016/j.jclepro.2012.10.049.
[4] Jaquin PA, Augarde CE, Gerrard CM. Chronological description of the spatial development of rammed earth techniques. Int J Archit Herit 2008;2:377–400. https://doi.org/10.1080/15583050801958826.
[5] Curto A, Lanzoni L, Tarantino AM, Viviani M. Shot-earth for sustainable constructions. Constr Build Mater 2020;239:117775.
[6] Franciosi M, Savino V, Lanzoni L, Tarantino AM, Viviani M. Changing the approach to sustainable constructions: An adaptive mix-design calibration process for earth composite materials. Compos Struct 2023:117143. https://doi.org/10.1016/j.compstruct.2023.117143.
[7] Vantadori, Żak S, Sadowski \Lukasz A, Ronchei C, Scorza D, Zanichelli A, et al. Microstructural, chemical and physical characterisation of the Shot-Earth 772. Constr Build Mater 2022;341:127766.
[8] A. D'Alessandro A. Meoni V. Savino M. Viviani F. Ubertini New self-sensing shot-earth cement-composites for smart and sustainable constructions: experimental validation on a full-scale vault Proc 6th Workshop N Bound Struct Concr 2022 Univ Salento - Acids Italy Chapter 2022.
[9] Tarantino AM, Cotana F, Viviani M, editors. Shot-Earth for an Eco-friendly and Human-Comfortable Construction Industry. Springer Nature Switzerland; 2023.
[10] Bacciocchi M, Savino V, Lanzoni L, Tarantino AM, Viviani M. Multi-phase homogenization procedure for estimating the mechanical properties of shot-earth materials. Compos Struct 2022;295:115799. https://doi.org/10.1016/j.compstruct.2022.115799.
[11] Minke G. Building with Earth: Design and Technology of a Sustainable Architecture. Walter. de Gruyter GmbH; 2021.
[12] Dobson S. Keynote papers Rammed earth in the modern world. Rammed Earth Construction. CRC Press; 2015.
[13] Savino V, Franciosi M, Viviani M. Engineering and analyses of a novel Catalan vault. Eng Fail Anal 2023;143:106841. https://doi.org/10.1016/j.engfailanal.2022.106841.
[14] Wardeh G, Ghorbel E, Gomart H, Fiorio B. Experimental and analytical study of bond behavior between recycled aggregate concrete and steel bars using a pullout test. Struct Concr 2017;18:811–25. https://doi.org/10.1002/suco.201600155.
[15] FIB-federation internationale du beton. CEB-FIP Model Code 1990: Design Code. Thomas Telford Ltd; 1993.
[16] FIB-federation internationale du beton. CEB-FIP Model Code for Concrete Structures 2010. Ernst & Sohn; 2013.
[17] Ciancio D., Beckett C. Rammed earth: an overview of a sustainable construction material 2013.
[18] Houben H, Guillaud H. Earth. Construction: A Comprehensive Guide. Reissue edizione. London: Practical Action Pub; 1994.
[19] CEN (European Committee for Standardization). Tests for geometrical properties of aggregates - Part 1. Determination of particle size distribution - Sieving method. Brussels, Belgium: CEN; 2012.
[20] SN-VSS. Identification des sols. Méthode de laboratoire avec classification selon l'USCS. Switzerland: Zürich; 1997.
[21] Bazant Z, Sener S. Size effect in pullout tests. Acids Mater J 1988;85:347–51.
[22] Bažant ZP. Size effect in blunt fracture: concrete, rock, metal. J Eng Mech 1984;110:518–35. https://doi.org/10.1061/(ASCE)0733-9399(1984)110:4(518).
[23] Padmanabham K, Rambabu K. Static pullout tests on retrofitted anchorage system in concrete using supplementary reinforcement. Saudi J Civ Eng 2022;6:79–94. https://doi.org/10.36348/sjce.2022.v06i04.004.
[24] Bayoumi E-S. Effect of hybrid fibers on bond strength of fiber reinforced concrete. ARPN J Eng Appl Sci 2020;15:2958–68.
[25] Freitas E, Louro AS, Costa H, Cavaco ES, Júlio E, Pipa M. Bond behaviour between steel / stainless-steel reinforcing bars and low binder concrete (LBC). Eng Struct 2020;221:111072. https://doi.org/10.1016/j.engstruct.2020.111072.
[26] CEN (European Committee for Standardization). Testing hardened concrete - Part 3: Compressive strength of test specimens. Brussels, Belgium: CEN,; 2003.
[27] Nawaz W., Elchalakani M., Karrech A., Australia W. Flexure Behaviour Of All Light Weight Reinforced Concrete Beams Externally Strengthened With CFRP Laminates n.d.
[28] Rydval M, Huňka P, Kolísko J. Dependence of Load Bearing Capacity on Homogeneity of Steel Fiber Distribution. Appl Mech Mater 2015;732:353–6.
[29] Lee HY, Jung WT, Chung W. Flexural strengthening of reinforced concrete beams with pre-stressed near surface mounted CFRP systems. Compos Struct 2017;163:1–12. https://doi.org/10.1016/j.compstruct.2016.12.044.
[30] Abdalla JA, Hawileh RA, Nawaz W, Mohammed A. Reinforced Concrete Beams Externally Strengthened in Flexure using Hybrid Systems. IEEE; 2018. p. 1–5.
[31] Godat A, L'Hady A, Chaallal O, Neale KW. Bond behavior of the ETS FRP bar shear-strengthening method. J Compos Constr 2012;16:529–39. https://doi.org/10.1061/(ASCE)CC.1943-5614.0000280.
[32] Swiss Society of Engineers and Architects. Swiss Standard SIA 262:2013: Concrete Structure. 2013.
[33] Khadka B, Shakya M. Comparative compressive strength of stabilized and unstabilized rammed earth. Mater Struct 2016;49:3945–55. https://doi.org/10.1617/s11527-015-0765-5.